International Journal of Wavelets, Multiresolution
and Information Processing
Vol. 4, No. 2 (2006) 227–238
© World Scientific Publishing Company

World Scientific
www.worldscientific.com

STUDY ON RELATIONSHIP BETWEEN CONDENSED PARTICLES AND STRUCTURE OF CONDENSATION JET USING 2D IMAGE AND DISCRETE WAVELETS MULTIRESOLUTION

MOTOAKI KIMURA* and MASAHIRO TAKEI
Department of Mechanical Engineering, Nihon University
1-8-14 Kanda Surugadai 101-8308 Tokyo, Japan
**kimura@mech.cst.nihon-u.ac.jp*

YOSHIFURU SAITO
Hosei University, 3-7-2 Kajino, Tokyo 184-0002, Japan

KIYOSHI HORII
Shirayuri College, 1-25 Midorigaoka, Tokyo 182-8525, Japan

This paper describes the application of discrete wavelet transforms to the analysis of condensation jets in order to clarify the associated fluid and heat transfer phenomena. An experimentally-obtained, two-dimensional image of the condensation particle density around the jet was decomposed into 7 levels of resolution with their respective wavelengths. Based on the known physical characteristics of turbulent flow around the jet, levels 0 and 1 were shown to represent the large-scale components of the condensation particle density and the higher levels represent the small-scale components. From the wavelet-analyzed images, the width of the condensation zone was obtained and this compared well with the width inferred from temperature measurements. Thus, the method was verified and also provided data not available experimentally.

Keywords: Visualization; discrete wavelet transform; jet diffusion; condensation; temperature.

AMS Subject Classification: 42C40, 58A20, 80A20

1. Introduction

The phenomena associated with condensation jets can significantly influence the flow and thermal efficiency of industrial equipment such as air conditioners, exhaust nozzles and piping for fluid transport.[1,2] By homogeneous condensation of the vapor phase, heat transfer to the surrounding fluid and a lowering of the local vapor pressure affect the flow fields of both phases. Further, the condensation water particles

*Corresponding author.

may produce undesirable effects such as corrosion on equipment surfaces. The purpose of this work is to improve the understanding of the physics behind condensation jets using wavelet-based visualization technique.

This paper also investigates condensation jets when a jet is submerged into another fluid. Kimura *et al.*[3] experimentally studied condensation jets formed when cold dry air is discharged downwards from a round nozzle into a high humidity environment. While this study provided visual data on condensation jet behavior, the details of the jet structure remain to be clarified.

Recently, wavelet analysis has gathered attention as an image processing technique for analyzing time spatial frequency characteristics.[4] Discrete wavelet analysis enables an image to be decomposed and regenerated numerically according to the orthonormal transform. Discrete wavelet transform has been applied, for example, by Saito[5] to an electromagnetic field calculation. Turbulent jets have also been analyzed with discrete wavelet multiresolution image analysis by Li *et al.*[6] The discrete wavelet analysis was therefore determined to be an appropriate technique for two-dimensional particle density imaging of the condensation jets, that is under consideration herein. The originality of this paper lies in the application of discrete wavelet multiresolution image analysis to the condensation jet image to further clarify the jet characteristics.

2. Experiment

2.1. *Experimental apparatus, procedures and conditions*

The test section was $300 \times 300\,\text{mm}^2$ in cross-section and 500 mm in length below the nozzle exit. It was built from Plexiglas for good visualization. The jet and the atmospheric air were supplied by two, separate air-supply systems. For the jet, a desiccant-type dryer with active alumina maintained the air from the compressor at a relative humidity of 1%. The jet issued into the test section from a nozzle of $d = 10\,\text{mm}$ in diameter. The mean jet temperature at the nozzle exit, T_o, was 0°C, and the mean exit velocity, U_o, was 4.5 m/s. For the surrounding high-humidity atmosphere, air was supplied from the compressor. The surrounding atmosphere temperature, T_e, was maintained at 40°C by heating this air supply prior to release into the test section. The high humidity air for the surrounding atmosphere was supplied to the test section at a flow rate high enough to entrain the cold dry jet air. Tests were conducted with relative humidity, ϕ, of 100% and 90%. For comparison purposes, a third test with jet discharge into dry air was also performed.

During the tests, the jet air was injected downward into the high humidity atmosphere and visual images were obtained with laser light sheet method. The laser light beam generated by the Argon laser was focused onto a sheet 1 mm in thickness by means of convex, cylindrical lenses. The digital image was captured with a CCD camera with an exposure time of 1.0 s. Jet velocities were measured with a laser-Doppler velocimeter in the forward-scattering mode. A chromel-alumel

thermocouple of 50 μm in diameter was used to measure the temperature. The thermocouple was coated with a thin silicone film in order to protect from current leakage by water droplets. The time constant of the thermocouple was 50 ms.

2.2. *Experimental results*

Figure 1 shows a photograph of the condensation jet by LLS and the CCD camera. The range of the photograph extends $r/d = \pm 4$ jet diameters in the radial direction and $z/d = 15$ diameters downward from the nozzle exit in the flow direction. r is the radial coordinate and z is the axial coordinate. The condensation zone clearly becomes wider with axial distance from the nozzle exit. Further, the radial cross-section of the condensation jet at a given distance downstream from the nozzle exit is smaller for the lower relative humidity.

Figure 2 shows the spatial temperature distributions, with all data obtained from the thermocouple and averaged over 1.0 s. The temperatures have been recast into dimensionless values as:

$$T_n = \frac{T - T_e}{T_e - T_o}. \tag{1}$$

Due to condensation and jet disintegration, the temperature change from the point of jet discharge ($T_o = 0°C$) to the surrounding temperature ($T_e = 40°C$) is clearly seen. From Fig. 2(a), the radial locations at which the temperature becomes equal to the surrounding temperature are $r/d = 1.4, 2.0, 2.5$ and 2.5 for $z/d = 4, 6, 8$ and 10, respectively. The radial location at which the temperature becomes equal to the surrounding temperature corresponds to the shear layer of the condensation jet (indicated by an arrow for $z/d = 4$). Within the region between the jet centerline and this location, the turbulent fluctuating component of the velocity is large and the intermittency coefficient is small. For this reason, condensation nucleation

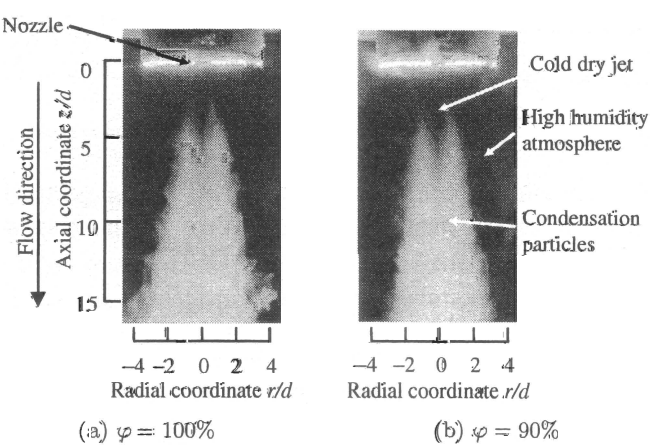

Fig. 1. Visualization of condensation jet.

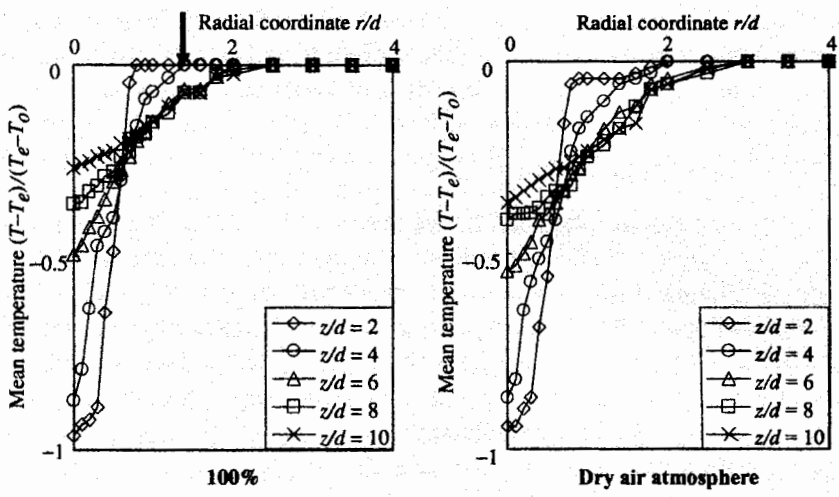

Fig. 2. Mean temperature distribution.

generation and evaporation coexist, and the condensation particle concentration fluctuates spatially.

In Fig. 2(b), the dew-point temperature (DPT) of 38°C, corresponding to 90% relative humidity, is shown. The radial locations at which the temperature becomes equal to the dew-point temperature are $r/d = 1.4, 2.0, 2.0$ and 2.0 for $z/d = 4, 6, 8$ and 10 respectively. Compared with the 100% relative humidity case, the jet is seen to be cooled to the dew-point temperature closer to the jet centerline.

3. Wavelet Multiresolution Decomposition of the Condensation Jet Image

3.1. *Resolution method*

The two-dimensional wavelet spectrum $\mathbf{S}$ is obtained by:

$$\mathbf{S} = \mathbf{WnXWm}^{\mathrm{T}}, \tag{2}$$

where $\mathbf{X}$ is the original image consisting of n pixel $\times$ m pixel elements, $\mathbf{Wn}$ ($n \times n$ elements) is an analyzing wavelet matrix and $\mathbf{Wm}^T$ is the transpose matrix of $\mathbf{Wm}$ ($m \times m$ elements). In this case, $\mathbf{X}$ is the CCD camera photograph of the condensation jet (Fig. 2). The inverse wavelet transform of Eq. (2) is:

$$\mathbf{X} = \mathbf{Wn}^{\mathrm{T}}\mathbf{SWm}. \tag{3}$$

In this study, we use the Daubechies basis with index $N = 16$, which is compact support, to analyze the flow image. When the Daubechies orthonormal function is used for analyzing the wavelets and the image data $\mathbf{X}$ is resolved with 256×512

data over the region (8 nozzle diameters $\times 16$ nozzle diameters), the original image can be decomposed to:

$$\begin{aligned}\mathbf{X} &= \mathbf{Wn}^{\mathrm{T}}\mathbf{S}\ \mathbf{Wm} \\ &= \mathbf{Wn}^{\mathrm{T}}\mathbf{S}_0\mathbf{Wm} + \mathbf{Wn}^{\mathrm{T}}\mathbf{S}_1\mathbf{Wm} + \mathbf{Wn}^{\mathrm{T}}\mathbf{S}_2\mathbf{Wm} + \mathbf{Wn}^{\mathrm{T}}\mathbf{S}_3\mathbf{Wm} \\ &\quad + \mathbf{Wn}^{\mathrm{T}}\mathbf{S}_4\mathbf{Wm} + \mathbf{Wn}^{\mathrm{T}}\mathbf{S}_5\mathbf{Wm} + \mathbf{Wn}^{\mathrm{T}}\mathbf{S}_6\mathbf{Wm}. \end{aligned} \tag{4}$$

$\mathbf{Wn}^{\mathrm{T}}\mathbf{S}_6\mathbf{Wm}$ is called level 6 and has the highest spatial resolution, while $\mathbf{Wn}^{\mathrm{T}}\mathbf{S}_0\mathbf{Wm}$ is called level 0 and has the lowest spatial resolution. The higher the level, the higher the spatial frequency it decomposes. The higher levels can visualize the particle density distribution without erasing the spatial information.

3.2. *Assumptions about condensation jet image and image decomposition*

By making some assumptions about the condensation jet images obtained experimentally, wavelet methods can be used to decompose the data into large-scale component images and small-scale component images. The phenomena under discussion can be better understood by referring to the condensation jet model shown in Fig. 3. Start with a typical point $\xi(r, z)$ inside the condensation jet region. Very small particles of diameter less than 0.01 μm form within the cooled dry jet and become condensation nucleation particles.

The brightness at a given $\xi(r, z)$ location is determined by the density of path lines followed by condensation particles for a period of 1.0 s. In other words, the

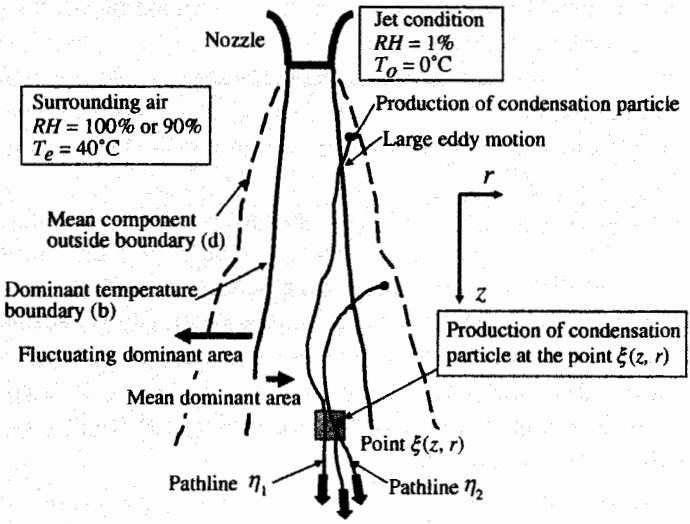

Fig. 3. Physical model for submerged condensation jet.

brightness is dependent on the nucleus formation rate on $\xi(r, z)$ point and at upstream positions, nucleus growth rate and movement velocities of condensation particles.

Injecting cold dry air into a saturated atmosphere produces the condensation jet. Condensation particles appear in the free shear layer because the local vapor saturation temperature has decreased to the dew-point temperature by jet-atmosphere mixing. This local energy addition and pressure decrease influence both the temperature fields and the flow in the jet core and surrounding layer.

The following assumptions are made about the condensation process:

1. By diffusive mixing into the test section, the cool dry jet issued into the high humidity atmosphere. The atmosphere is locally and instantaneously cooled down to the dew-point temperature. At this instant, latent heat is released and condensation nuclei are formed.
2. The nucleation rate is only dependent on thermodynamic phenomena. That is, the effect of any extremely small particles that were not initially filtered out of the cool dry air can be ignored.
3. Upon formation, the nucleation particles are large enough to be considered condensation nucleation sites.
4. The jet average velocity and turbulence intensity do not affect the condensation particle concentration within a pixel. Condensation particles formed within a pixel pass through the pixel due to sufficient velocity and shutter opening time (1.0 s).
5. The temperature distributions in the $z-r$-plane are determined by heat transfer between the jet and surrounding fluid and heat release from condensation.
6. The change of absolute temperature in the jet diffusion region is larger than the change in other variables within the jet diffusion region.

Using the above physical model assumptions, condensation particle density $C(r, z)$ of ξ point is expressed by:

$$C(r,z) \approx k \int_0^{t1} J(T(r,z))dt + k \int_0^{t1} \int_0^{\eta} J(T(\xi)) \cdot d\xi \, dt. \tag{5}$$

Here, r is the radial distance from the nozzle center, z is the distance from the nozzle outlet in the flow direction, k is a fixed number for the sensitivity of the CCD camera to the exposure, t_1 is the exposure time (1.0 s in this study), and η is a position vector on a path line that passes through the point. According to the nucleation theory of Volmer,[8] the nucleation rate J per unit time and volume is given by (Delale[7]):

$$J = \sqrt{\frac{2}{\pi}} \sigma_\infty m^{-1.5} \frac{\rho_v^2}{\rho_c} \exp\left(-\frac{16}{3} \pi \frac{\sigma_\infty^3}{m \rho_c^2 R_v^3 T^3 \ln^2(S)} \right). \tag{6}$$

Here, σ_∞ is surface tension, m is mass per molecule, ρ_v is steam density, ρ_c is condensate density, R_v is the specific gas constant, T is absolute temperature in the jet diffusion domain as a function of r and z, and S is the relative humidity.

$$S = \frac{p'_v}{p'_{vs\infty}(T)}. \tag{7}$$

Here, p'_v is steam partial pressure and, $p'_{vs\infty}(T)$ is saturated steam partial pressure. In Eq. (5), the first term represents the generation of condensation particles at the point ξ and the second term is the generation of condensation particles passing through the position ξ from upstream. The brightness of the condensation jet image can be decomposed into a steady component and a fluctuating component:

$$\begin{aligned} C(z,r) &= \overline{C(z,r)} + c'(z,r) \\ &= \left\{ k \int_0^{t1} \overline{J(T(z,r))} dt + k \int_0^{t1} \int_0^{tl} \overline{J(T(\xi))} \cdot d\xi \, dt \right\} \\ &\quad + \left\{ k \int_0^{t1} \overline{J'(T(z,r))} dt + k \int_0^{t1} \int_0^{\eta} \overline{J'(T(\xi))} \cdot d\xi \, dt \right\}. \end{aligned} \tag{8}$$

In Eq. (8), the brightness of the condensation jet image consists of the steady components due to the nucleation rates which are constant with time, $\overline{J(T(r,z))}$ and $\overline{J(T(\xi))}$, and the components of the nucleation rates which fluctuate in time, $\overline{J'(T(r,z))}$ and $\overline{J'(T(\xi))}$.

The length scale of large eddy motion in the free shear layer of the jet is estimated to be about 20 mm. $\overline{C(r,z)}$ is assumed to be equivalent to the summation of wavelet levels 0 and 1, and $c'(r,z)$ taken to be equivalent to the summation of wavelet levels 2 through 6.

Figure 4 describes a condensed particle concentration relating to temperature distribution and jet stricture within two important broader area; that is, the temperature dominating layer within large-structure levels 0–1, the coherent structure and dominating turbulent mixing process in the shear layer within small-structure levels 2–6.

Figure 4 shows the large-scale component image of the condensation jet image calculated from the summation of wavelet levels 0 and 1. Figure 4 shows the small-scale component image from the summation of wavelet levels 2 through 6. The condensation particle density is indicated by a ten-level gray scale from black (low density) to white (high density). This visualizes the two-dimensional image of the normalized steady intensity in the zone of $r/d = 0$ to 4 and $z/d = 0$ to 10. This is the two-dimensional image of the normalized fluctuation intensity. From Fig. 4, the major component of the condensation particle density can be extracted clearly. It is thought that there are the small-scale component image of the condensation particle density in Fig. 4 and some relation as for the boundary of the zone where condensation particle are produced.

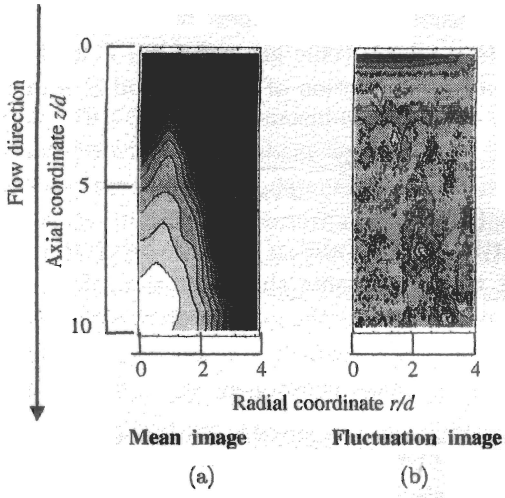

Fig. 4. Mean image and fluctuation image decomposed from the condensation original image.

4. Discussion

4.1. *Wavelet level and condensation particle density distribution*

Figure 5 shows cross-sectional slices of the two-dimensional image of the normalized steady intensity component from Fig. 4 at four axial positions, $z/d = 4, 6, 8$ and 10, for the case of 100% relative humidity. From these figures, the peak is noted to move inward toward the centerline with distance from the nozzle outlet. The peak normalized intensity is also noted to increase from 0.58 to 0.88 with distance from nozzle outlet. Further, the outer boundary of the region containing the steady

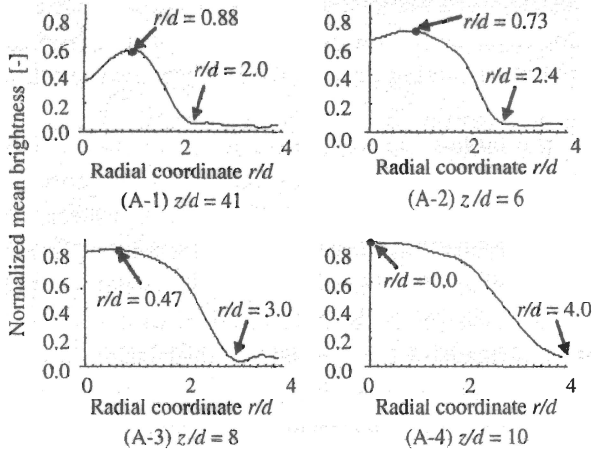

Fig. 5. Normalized large-scale intensity distribution at low wavelets level (100%).

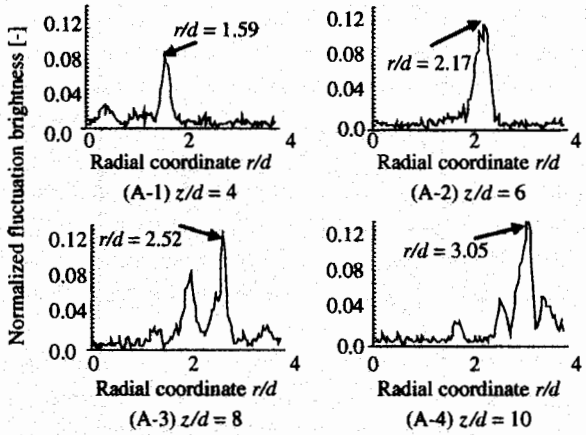

Fig. 6. Normalized fluctuation intensity distribution at high wavelets level (100%).

component moves radially outward, indicating a radially spreading of the condensation jet. The outer boundary increases from $r/d = 2.0$ at $z/d = 4$ to $r/d = 4.0$ at $z/d = 10$.

Figure 6 shows cross-sectional slices of the two-dimensional image of normalized fluctuating intensity component from Fig. 4(b) at four axial positions, $z/d = 4, 6, 8$ and 10. We are able to think that the highest peak in the cross-section of the wavelet-composed result is adapted to the intensive distribution change of condensation particle density. In contrast to the peaks of the steady intensity component, the peaks of the fluctuating intensity component move outward with distance from the nozzle. This peak position (b) corresponds to the boundary location in the radial direction with average nucleus generation rates of $\overline{J(T(r,z))} + \overline{J(T(\xi))}$ for the steady component and $J(T(r,z)) + J'(T(\xi))$ for the fluctuating component. The position (b) is used with Fig. 6. The steady boundary and the fluctuating boundary are shown in Fig. 3 by a solid and a dotted line, respectively. A main outcome of this work, the steady and fluctuating components of the condensation jet image were successfully decomposed into a steady component image and a fluctuating component image using wavelet multiresolution techniques. Further, the boundaries of the regions containing primarily steady temperatures and primarily fluctuation temperatures were identified and the outer boundaries of the regions containing the steady concentration of condensation particles were also shown.

4.2. *Steady and fluctuating temperature component regions and outer boundary of the jets*

Using wavelet multiresolution methods to decompose the steady and fluctuating components of a condensation jet, the boundaries of the steady and fluctuation temperature regions and the steady component outer boundary have been identified.

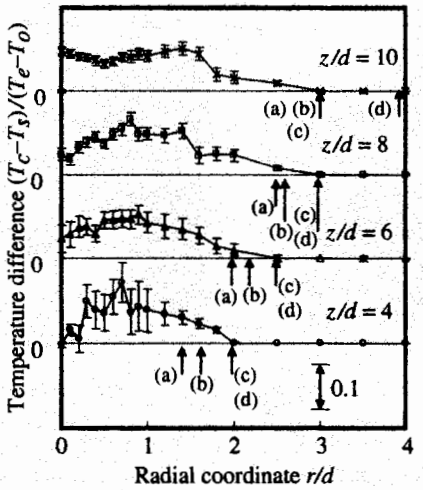

Fig. 7. Mean temperature distribution in radial-wise.

In this section, the reasonableness of the results is discussed. Figure 7 shows the difference of the steady temperature distributions for the condensation jet and the jet issued into dry air, as obtained from experimental data of Fig. 2. Here, T_c is the temperature of condensation jet, T_s is the temperature of the single-phase jet, T_e is the atmospheric temperature (40°C), and T_o is the exit temperature (0°C). The solid line in Fig. 7 corresponds to the sum of the nucleation particle generation rate at point ξ, $\overline{J(T(r,z))}$ and the generation of condensation particles passing through the position ξ from upstream, $\overline{J(T(\xi))}$, from Eq. (10). Figure 7 is the radius position at which the dew-point temperature of Fig. 2 was reached (hereinafter referred to as the dew-point position), (b) is the dominant mean temperature boundary position the temperature dominant layer position in Fig. 6, (c) is the position at which the average temperature of the condensation jet and the non-condensing jets of Fig. 7 becomes equal (hereinafter referred to as the circumference temperature arrival position), and (d) is the position of greatest circumference in Fig. 5. "0" in Fig. 7 shows the starting point of $(T_c-T_s)/(T_e-T_o)$ in each section. "0.1" in Fig. 7 shows the scale of "temperature difference" $(T_c-T_s)/(T_e-T_o)=0.1$.

The temperature dominant layer position (b) is located outside the dew-point position (a). This is thought to be because the dew-point position (a) shows the position of time average to reach the dew-point temperature, when actually, a fluctuation of intermittent flow by coherent structure is produced in the free shear layer. Accordingly, through the mixture of high-humidity circumference air and cold air, condensation particles form by falling below the dew-point temperature intermittently at a position outside the dew-point position (a). More concretely, for $z/d=4$ to 8 in Fig. 7, because the dew-point position (a) fluctuates considerably,

the temperature dominant layer position (b) is located outside the dew-point position (a). However, downstream at $z/d = 9$, the temperature dominant layer position (b) becomes a radius position identical to the dew-point position (a) because there is no temperature fluctuation of the dew-point position (a).

In addition, the temperature dominant layer position (b) is located inside the circumference temperature arrival position (c). This is thought to be because in the region outside the temperature dominant layer position (b) "sensible heat" is discharged intermittently by the creation of an intermittent condensation particle, and this sensible heat causes the region to reach the circumference temperature arrival position (c).

Furthermore, the position of greatest circumference (d) is located at or outside the circumference temperature arrival position (c). The creation of a condensation particle is not possible outside the circumference temperature arrival position (c) of Fig. 7. However, it is thought that the path line of the condensation particle was recorded as an image because the condensation particle which occurred upstream was guided by a vortex structure in the free shear layer and was transported to the circumference region downstream. Because the influence of transport to the circumference region of this condensation particle is small upstream in the range of $z/d = 4$ to 6, there is not a large difference between the position of greatest circumference (d) and the circumference temperature arrival position (c). But the position of greatest circumference (d) is located outside the circumference temperature arrival position (c) because the influence of transport to circumference region of this condensation particle is large downstream in the range of $z/d = 8$ to 10.

5. Conclusions

Discrete wavelet transforms have been successfully applied to the analysis of condensation jets in order to improve understanding of the complicated fluid and heat transfer phenomena.

1. In order to visualize the path line densities of condensation particle distributions, the path line densities were resolved into multiple frequency bands.
2. The component of the condensation particle spatial distributions that did not fluctuate in time was defined as the summation of wavelet levels 0 and 1. The fluctuating component of the condensation particle distributions is equivalent to the summation of the higher levels, wavelet levels 2 through 6.
3. By multiresolution, the components of the jet structure have been quantitatively separated and valuable data which is not available from experiment has been obtained.
4. The edge of the condensation zone may be inferred from the fluctuating component images. Comparison against experimental data verified that the wavelet analysis techniques showed the same condensation region as was experimentally observed.

5. The qualitative understanding of the condensation jet gained from wavelet analysis may be used to aid in development of numerical models for the physics of the jet.

References

1. G. H. Schnerr and U. Dohrmann, Transonic flow around airfoils with relaxation and energy supply by homogeneous condensation, *AIAA J.* **28**(7) (1990) 1187–1193.
2. A. B. Vatazhin, A. Y. Klimenko, A. B. Lebedev and A. A. Sorokin, Effect of turbulent fluctuations on homogeneous condensation in a turbulent isobaric submerged jet, *Fluid Mech. Soviet Res.* **20**(2) (1991) 1–11.
3. M. Kimura, K. Itho, K. Ono and A. Saima, The study of cold jet issuing into high humidity environment, *Proc. ASME/JSME Thermal Eng. (Hawaii)* (1995) 165–170.
4. R. K. Young, *Wavelets Theory and its Applications* (Kluwer Academic Publications, USA, 1993).
5. Y. Saito, Wavelet analysis for computational electromagnetics, *Trans. Inst. Electr. Eng. Jpn. A* **116**(9) (1996) 833–839 (in Japanese).
6. H. Li, M. Takei, M. Ochi, Y. Saito and K. Horii, Application of two-dimensional orthogonal wavelets to multiresolution image analysis of a turbulent jet, *Trans. Japan Soc. Aero. Space Sci.* **42**(137) (1990) 120–127.
7. C. F. Delale, M. J. E. H. Muitjens and M. E. H. van Dongen, Asymptotic solution and numerical simulation of homogenous condensation in expansion cloud chambers, *J. Chem. Phys.* **105**(19) (1996) 8804–8821.
8. M. Volmer, *Kinetik der Phasenbildung* (Stienkopff-Verlag, Leipzig, Germany, 1939).